

Dopant size effect on BiFeO_3 perovskite structure for enhanced photovoltaic activity

Tewodros Eyob,^{1, a)} Kenate Nemera,^{1, b)} and Lemi Demeyu^{1, c)}

Department of Physics, Addis Ababa University, P.O. Box 1176, Addis Ababa, Ethiopia

(Dated: 10 May 2022)

This study is carried out using first principles density functional theory calculations within gpaw code. Atomic size effect is analyzed and investigated by doping either Li, Cs or both on Barium doped BiFeO_3 (BFO) which belongs to monoclinic $P2_1/m$ space group. The calculated results reveal that Cs doped BFO had significantly improved photocurrent density seemingly due to broadened absorption peaks & biplasmons generation. Codoping two atoms with large size difference have a significant effect on plasmon width & peak than doping with a single & small sized atom. At higher photon energy realms of the order 10 eV, the index of refraction reduces to $n(\omega) \rightarrow 1$ implying that light wave can tunnel through the pristine & doped BFO without any phase change, thus indicating its potential as an efficient candidate for a photonic application. In addition, doped BFO shows abundant photocurrent generation properties which would be important in solar cell & photovoltaic applications.

Keywords: Bismuth ferrite, Density functional theory, Photoelectron, Photovoltaic, Multiferroic, Optical band gap.

I. INTRODUCTION

BiFeO_3 (BFO) is multiferroic perovskite crystal structure, which permits coexistence of various orders at room temperature. Doping fine or large sized atoms further improves simultaneous coexistence of different orders in single phase resulting in enhanced structural, optical and electronic properties of materials¹.

Several attempts have been done in advancement of the ferromagnetic properties of BFO & for improvements in leakage current amount decrement by doping either in A-site or B-site or both sites². Shaan Ameer et al³ reported that doping Li on BFO reduces ferromagnetism. However, optical property enhanced due to small optical band gap energy. Moreover, Aungkan Sen et al⁴ suggested proportional doping of Ba & Mo in BFO result in improved optical absorbance and dielectric property.

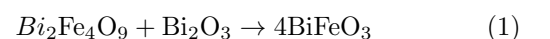
Highest level of doping not only alter the properties of the materials, but had remarkable impact on the crystal structure as well. For instance, La-doped BFO structure is transformed from rhombohedral to triclinic or orthorhombic around 10 mol %, and a smaller ionic radius rare-earth doping at the B-site causes structural distortion, and brought forth antiferroelectric-like double-hysteresis P-E loops. Moreover, rare-earth elements with a smaller ion radius, because of a geometrical & magnetic moments factor, are forced to align themselves either in symmetrical or antisymmetrical orientation, resulting in various magnetic order phases. Arnold et al⁵ also ascertained that rare-earth doped BFO materials' ionic radii at B-site are the prominent source for phase transitions

and structural phase transitions, which is also supported by other literatures⁶⁻⁸.

Besides phase, structural and property alteration, chemical strain forces can be exhibited among atoms because of short and long range interactions. J.A. Schiemer et al⁹ studied significance of strain in coupling phase orders with effect on elastic response of either in high or low level doped crystals in relation to magnetic order, oxygen vacancy dynamics, and conductivity. It is also inferred that important transformation in multiferroic properties are highly correlated to structural changes. It has been well understood that applied strain on BFO scales up the magnetic, piezoelectric, ferroelectric, and optical properties¹⁰.

Liang Bai et al¹¹ also experimented and observed that doping Co^{3+} ions knocks out Fe^{3+} ions from B-sites and opens up for random substitute. Consequently, a spirally arranged spin becomes disrupted and chemical strain is grown because of uneven size of the two B-site cations (Co^{3+} and Fe^{3+} ions). In spite of the previous efforts, strain evolution due to dopant size & its facilitation for coupling of multiferroic orders still remains debatable. Here we considered perovskite monoclinic BFO ($P2_1/m$) phase & the experimentally synthesized counterpart as heated over a range of high temperature during sintering processes, is evidenced with appearance of several phases plus parasitic phase ($\text{Bi}_2\text{Fe}_4\text{O}_9$)¹².

In the course of sintering process, various transformation is undergone as function of temperature leading to bismuth depreciated, due to its volatility resulting in impure BFO phases, which is often called secondary phase of the cubic structure. However, these phases are further purified by proportional addition of Bi_2O_3 and Fe_2O_3 ¹³, see Eq. (1).



^{a)}Electronic mail: tewodros.eyob@aau.edu.et

^{b)}Electronic mail: kenate.nemera@gmail.com

^{c)}Electronic mail: lemi.demeyu@aau.edu.et

We considered perovskite monoclinic BFO ($P2_1/m$) phase because one could easily understand doping effect. Therefore, this work explores cesium (Cs) and lithium (Li) size effect on barium (Ba) doped BiFeO₃. It results in structural phase transition due to strain created because of size of substitute atoms (Fig. 1).

II. COMPUTATIONAL METHOD

Ab initio calculations were performed using the projector augmented wave (PAW) method as implemented in *gpa* code¹⁴. The electron wave-function is approximated using the implementation of a projector augmented wave method¹⁵ & the Schrödinger equation applied to total energy functions are solved self-consistently using the Kohn-Sham scheme¹⁶. All electron waves are expanded over periodic potential plane with a method of P.E. Blöchl¹⁷ having a band, a k -points, and a reciprocal lattice grid indices. A plane wave cut-off energy used is 520 eV. The k -points within Brillouin zone (BZ) is chosen according to Monkhorst-Pack scheme¹⁸, where a \mathbf{k} -mesh of $8 \times 8 \times 8$ is used.

The interactions of the valence electrons with the core electrons and nuclei is treated within a projector augmented wave (paw) data sets^{14,15}. The number of valence electrons considered for each element within the paw data sets is Bi ($5d^{10}6s^26p^3$), Fe ($3d^64s^2$), O ($2s^22p^4$), Cs ($5s^25p^66s^1$), Li ($2s^1$), & Ba ($5s^25p^66s^2$). Geometry relaxations are carried out using BFGS minimizer¹⁹, where optimizations of the atomic coordinates and the unit cell degrees of freedom is done within the concept of the Hellmann-Feynman forces and stresses^{20,21} calculated on the Born-Oppenheimer (BO) surface²². The convergence criteria for the forces were set at 0.05 eV/Å. The exchange-correlation energies are approximated within the generalized gradient approximation of PBE²³ & a \mathbf{k} -mesh of $8 \times 8 \times 8$ is used in a geometry relaxation calculations. The strongly correlated nature of d electrons of Fe were treated using Hubbard-like model which is introduced into the *Gpa* code according to^{24,25}, where $U-J=7.5$ eV.

Brillouin zone integration were performed with the tetrahedron method which is proved efficient especially for excited states & magnetically induced dielectric function calculation²⁶. Ground state calculation is performed with k -point density of 5 points per Å⁻¹ with Γ -point inclusion. A restarted calculations were done with a fixed density of 7.5 points per Å⁻¹ over densely sampled k -points grid. The k -point density is calculated as:

$$N \frac{\mathbf{a}^*}{2\pi} \quad (2)$$

where N is the number of k -points and \mathbf{a}^* is the reciprocal of a lattice vector \mathbf{a} of the unit-cell. One can analyse and understand material's optical response property once incident photon energy is imparted to the electron, where

the material's response or dielectric function is given as

$$\varepsilon(\omega) = \varepsilon_1(\omega) + i\varepsilon_2(\omega) \quad (3)$$

The imaginary part $\varepsilon_2(\omega)$ is calculated from the density matrix of the electronic structure²⁷ according to the implementations by the group of G. Kresse^{28,29}, & given by

$$\varepsilon_2(\omega) = \frac{2e^2}{\Omega\omega^2m_e^2} \sum_{\mathbf{k},v,c} w_{\mathbf{k}} |\langle \psi_{\mathbf{k}}^c | \mathbf{u} \cdot \mathbf{r} | \psi_{\mathbf{k}}^v \rangle|^2 \delta(E_{\mathbf{k}}^c - E_{\mathbf{k}}^v - \hbar\omega), \quad (4)$$

where e is the electronic charge, and $\psi_{\mathbf{k}}^c$ and $\psi_{\mathbf{k}}^v$ are the conduction band (CB) and valence band (VB) wave functions at \mathbf{k} , respectively, $\hbar\omega$ is the energy of the incident phonon, $\mathbf{u} \cdot \mathbf{r}$ is the momentum operator, $w_{\mathbf{k}}$ is a joint density of states, & Ω is volume of the primitive cell.

The Real part $\varepsilon_1(\omega)$ of the dielectric function can be found from the Kramer-Kronig equation³⁰.

$$\varepsilon_1(\omega) = 1 + \frac{2}{\pi} P \int_0^\infty \frac{\omega' \varepsilon_2(\omega') d\omega'}{\omega'^2 - \omega^2} \quad (5)$$

where, P stands for the principal value of the integral. The optical absorption coefficient was obtained by using Eq. (6)

$$\alpha = \sqrt{2} \frac{\omega}{c} \sqrt{\varepsilon_1^2(\omega) + \varepsilon_2^2(\omega) - \varepsilon_1(\omega)} \quad (6)$$

where ω is photon frequency, c is speed of light. ε_1 & ε_2 are frequency dependent real and imaginary parts of dielectric function as stated in Eq. (3). For photovoltaic applications, the BFO should be able to absorb as much light as possible to generate a photocurrent, which requires a lower band gap and a large absorption coefficient.

The photocurrent density under irradiation with a certain wavelength can be described by an empirical Glass Law³¹.

$$J_{ph} = \alpha \kappa I \quad (7)$$

where α is the optical absorption coefficient, κ is a material-dependent Glass coefficient, and I is irradiation intensity. The photocurrent density J_{ph} is linearly proportional to the absorption coefficient. The relation between α and an optical band gap E_g^o can be estimated using the Tauc relation³².

$$\alpha(\hbar\omega) \sim A(\hbar\omega - E_g^o)^{\frac{1}{2}} \quad (8)$$

where A is a material dependent constant and $\hbar\omega$ is the incident photon energy. According to Eq. (7) & Eq. (8), one can extrapolate a larger photocurrent density by increasing the absorption coefficient with a small band gap.

From dielectric function, all the other optical properties such as, reflectivity R , refractive index n_0 , & extinc-

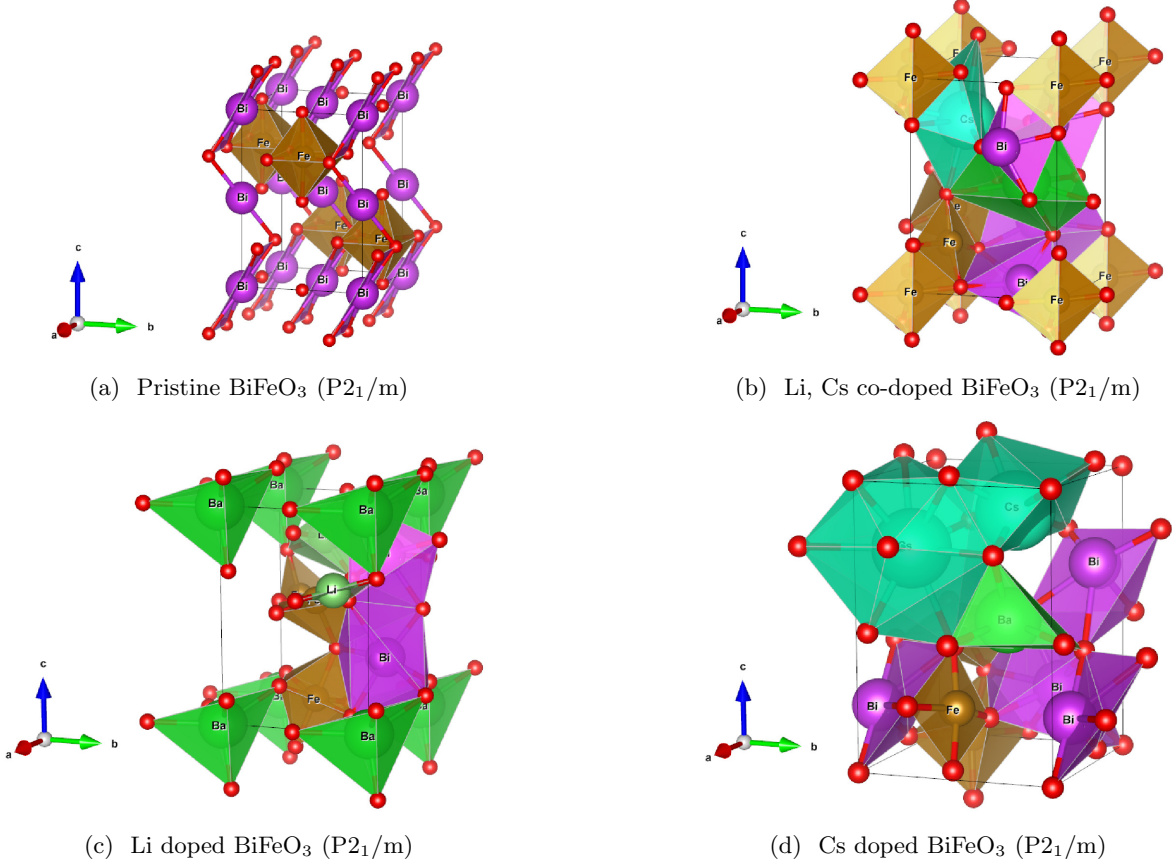


FIG. 1: Color online. Crystal structure of bulk pristine BiFeO₃ in comparison with doped BiFeO₃ illustrating the structural tilting of BiO₆ polyhedra relative to neighbouring polyhedrons.

tion coefficient κ is also obtained^{33–35}, & given as follows.

$$n(\omega) = \frac{1}{\sqrt{2}} \sqrt{\sqrt{\varepsilon_1^2(\omega) + \varepsilon_2^2(\omega)} + \varepsilon_1(\omega)} \quad (9)$$

In addition, reflectivity $R(\omega)$, & energy loss function $\iota(\omega)$ is calculated as

$$R(\omega) = \left| \frac{\sqrt{\varepsilon(\omega)} - 1}{\sqrt{\varepsilon(\omega)} + 1} \right|^2 \quad (10)$$

and

$$\iota(\omega) = \frac{\varepsilon_2(\omega)}{\left[\varepsilon_1^2(\omega) + \varepsilon_2^2(\omega) \right]}, \quad (11)$$

respectively.

The spin-orbit module calculates spin-orbit band structures non-self consistently. The input is a standard converged GPAW calculation and the module diagonalizes the spin-orbit Hamiltonian in a basis of scalar-relativistic Kohn-Sham eigenstates. Since the spin-orbit coupling is largest close to the nuclei, we only consider

contributions from inside the PAW augmentation spheres where the all-electron states can be expanded as

$$|\psi_{nk}\rangle = \sum_{ai} \langle \tilde{p}_i^a | \tilde{\psi}_{nk} \rangle | \phi_i^a \rangle \quad (12)$$

The full Bloch Hamiltonian in a basis of scalar relativistic states becomes

$$H_{nn'\sigma\sigma'}(\mathbf{k}) = \varepsilon_{nk\sigma} \delta_{nn'\sigma\sigma'} + \langle \psi_{nk\sigma} | H^{SO}(\mathbf{k}) | \psi_{n'k\sigma'} \rangle = \varepsilon_{nk\sigma} \delta_{nn'\sigma\sigma'} + \sum_{i_1 i_2} \langle \tilde{\psi}_{nk} | \tilde{p}_{i_1}^a \rangle \langle \phi_{i_1} \sigma | H^{SO}(\mathbf{k}) | \phi_{i_2} \sigma' \rangle \langle \tilde{p}_{i_2}^a | \tilde{\psi}_{n'k} \rangle \quad (13)$$

where the spinors are chosen along the z-axis as default. It is also possible to obtain the eigenstates of the full spin-orbit Hamiltonian as well as the spin character along the z-axis. The spin character is defined as

$$s_{mk} \equiv \langle mk | \sigma_z | mk \rangle \quad (14)$$

and is useful for analysing the degree of spin-orbit induced hybridization between spin up and spin down states³⁶.

III. RESULTS AND DISCUSSION

Experimental refined x-ray diffraction structural positions were obtained from Inorganic Crystal Structure Database (ICSD)³⁷. Structural volume optimization made over lattice range 5.0 Å to 6.0 Å, and obtained $a(\text{Å}) = 5.5803663$, $b(\text{Å}) = 7.9236074$, & $c(\text{Å}) = 5.6120707$, and $\alpha(^{\circ}) = 90$, $\beta(^{\circ}) = 90$, & $\gamma(^{\circ}) = 90.015$ which are in close agreement to experimental parameters. The bulk modulus at monoclinic $P2_1/m$ space group (Fig. 1) is found to be $B = 161.582$ GPa, & also shown weak ferromagnetism with average a remnant magnetization of $3.5 \times 10^{-6} \mu_B/\text{Fe}$. This value is close to literature value $4 \times 10^{-6} \mu_B/\text{Fe}$ ³⁸.

Band structure is calculated in Fig. 2 using spin-orbit coupling module as implemented in the Gpaw electronic structure code, & plotted over special k-points which were exported online according to a literature³⁹ by inputting the crystallographic information file of $P2_1/m$ space group.

The calculated absorption coefficient $\alpha(\omega)$ of pristine compared with doped bismuth ferrite are shown in Fig. 3. The absorption ability seems to be reduced for all doped systems compared to pristine BFO in low energy-loss region. In addition, the optical bandgap is significantly decreased as illustrated in the Table. I, but a dopant size also seems to have an effect on the optical gap (Fig. 2).

The imaginary part, $\varepsilon_2(\omega)$ (Fig. 3) shows absorption peaks in a photon energies range of 0.0-10.0 eV. The imaginary part is associated with only inter-band transition, and the real part $\varepsilon_1(\omega)$ approaches to zero at certain realms of photon energies, signaling a resonance at which collective electrons start to excite at plasma frequency. It looks from Fig. 2 that a congested bound of bands near the Fermi level of valence band seems to oscillate with plasma frequency. From Fig. 4, the optical bandgaps presented in the Table I are calculated using Tauc relation (Eq. (8)), & according to a tangent line curve fitting approach adopted from a literature⁴⁰.

We also notice from Figs. 4 & 5 that absorption peaks occur over a wider ranges of photon energies by doping the BFO, & that a decrease in the imaginary part $\varepsilon_2(\omega)$ at higher photon energy potentially indicates a decline in absorption of photon energy to bound electron of valance band. Thus, the excitation of the plasmons by light is demonstrated by a decrease of the reflectivity $R(\omega)$ of the light at plasma frequency because of photon energy is consumed up by oscillating bound electrons. The refractive index as indicated in Fig. 5 show that $n(\omega) \rightarrow 1$, at high photon energies (~ 10 -15 eV). This could potentially imply that light can pass through the material without a phase change, which is a novel characteristics of photonic crystals. Such a claim also agrees with experimental & theoretical concepts explained in literature^{41,42}.

As shown in Fig. 6, plasmons move in a periodic potential and unlike ideal plasmons, and pristine BFO, had three peaks at 10 eV, 19 eV & 27 eV. Li & Cs co-doped BFO had three peaks at 21 eV, 24 eV, & 27 eV.

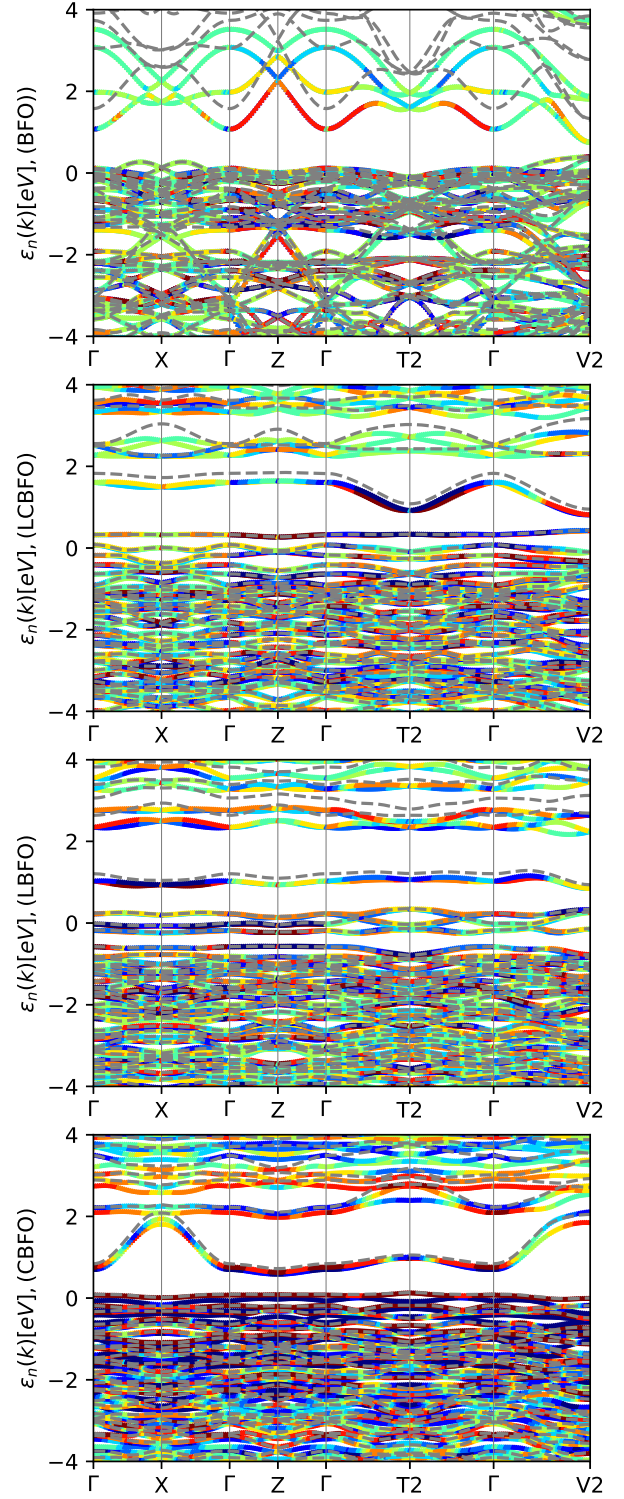


FIG. 2: Scatter spin-orbit coupled band structure calculated using Eq. (14). The colors show the spin character: blue designated as spin down, red as spin up and dashed gray lines as bands without spin-orbit coupling respectively. (For color online, the reader is referred to the web version of this article).

TABLE I: Calculations of magnetization, optical band gap energy, & magnetic moment contribution per Fe atom, is given. Wherever it applies in this paper, BFO means pristine BiFeO₃, LiCs-BFO means Li & Cs co-doped BFO, Li-BFO means Li doped BFO, & Cs-BFO means Cs doped BFO.

System	Magnetization [μ_B]	Optical band gap [eV]	Moment per Fe-atom [μ_B/Fe]
BFO	1.5×10^{-6}	2.13275	4×10^{-6}
LiCs-BFO	0.000	0.6855	0.000
Li-BFO	2×10^{-6}	0.7125	1×10^{-6}
Cs-BFO	1.532450	0.6746	0.71731

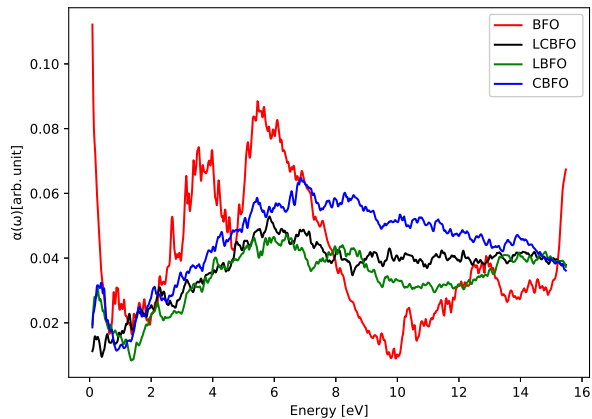


FIG. 3: The absorption coefficient $\alpha(\omega)$ for pristine BiFeO₃ in comparison to doped BiFeO₃. (For color online, the reader is referred to the web version of this article).

Li doped BFO had two peaks at 21 eV, & 28 eV. Cs doped BFO had three peaks at 15 eV, 26 eV, & 28 eV. The energy-loss may show plasmon excitation in region of about 10-30 eV often during inter-band transition of single electron. However, high energy-loss region is highly associated with excitation of bound electron with multiple peaks. These bound electron significantly increase photocurrent generation which enormously enhance photovoltaic effect. It is been noted that two plasmons of pristine BFO interact via electron-hole pair resulting in biplasmons generation due to Cs doping. However, Li doping affected the amount of energy of the two peak points plus a very small peak at 30 eV. Therefore, Cs size had effect on biplasmons generation in comparison to the Li size. In some cases, plasmons width & peak explain the phase changes. We can infer that size of the dopant atom has remarkable impact on both number & width of plasmons resulting in enhanced photovoltaic property. Hence, co-doping of Li & Cs in a Barium doped bismuth ferrite seems to have a potential for improved efficiency as a photoelectron capturing device.

IV. CONCLUSION

The investigations can be summarized as follows.

- With doping, absorption coefficient has widened resulting to a decreased optical bandgap & hence shows a potential for an increased solar cell property.
- A squared absorption coefficient peak shows an increase in width of by about 4 eV towards a realm of higher photon energies in the case of doped BFO. This is believed to be a sign of an increased solar cell activity.
- Dielectric functions seem to have large values at zero photon energies, but these values seem to be reduced significantly by an introduction of a series of photon energies of up to $\hbar\omega=10$ eV. For photon energies of 10-15 eV, $n(\omega) \rightarrow 1$.
- The crossing of the imaginary part of the dielectric function $\varepsilon_1(\omega)$ of a zero values at multiple realms of the photon energies $\hbar\omega$ indicates a potential importance of the system in applications based on photonic conductivity.
- The systems' $\varepsilon_1(\omega)$, $\varepsilon_2(\omega)$, & $n(\omega)$ seem to be reduced rapidly with introduction of photon energies, while a major contributor to the magnitude of $n(\omega)$ seems to be $\varepsilon_2(\omega)$.
- Expanded width of energy loss peaks happen with doping & an occurrence of such peaks at higher photon energies indicates a potential importance for applications in a plasmonic effect.

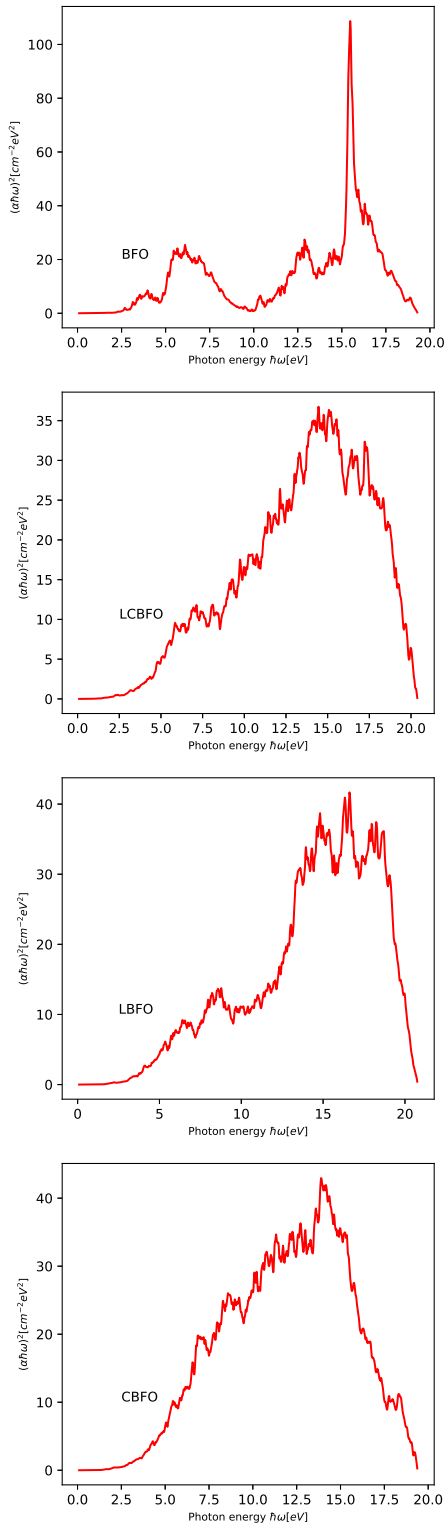


FIG. 4: Tauc plots $(\alpha\hbar\omega)^2$ vs. photon energy $\hbar\omega$ for direct band gap E_g^o extrapolation or estimation of pristine BFO, Li & Cs co-doped BFO, Li doped BFO, & Cs doped BFO in respective order of from top to bottom.

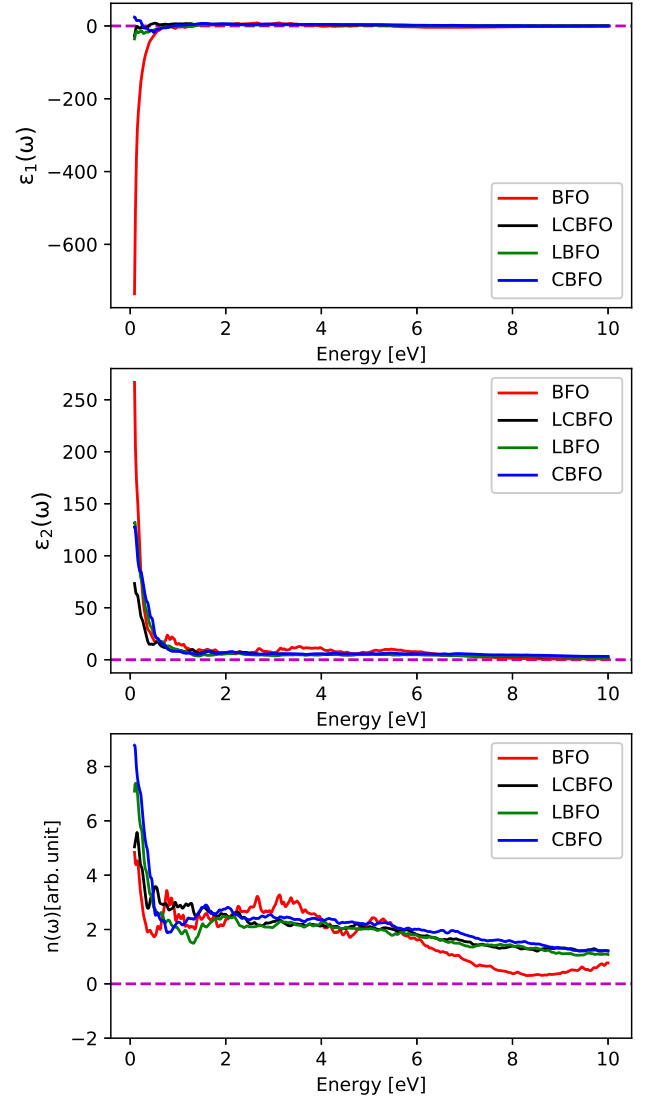


FIG. 5: The calculated real part $\varepsilon_1(\omega)$ and imaginary part $\varepsilon_2(\omega)$ of dielectric function $\varepsilon(\omega)$ & refractive index $n(\omega)$ in pristine BiFeO_3 , compared with doped BiFeO_3 . (For color online, the reader is referred to the web version of this article).

DISCLOSURE STATEMENT

The authors declare that there is no conflict of interest.

DATA AVAILABILITY STATEMENT

The data that support the findings of this study are available upon reasonable request from the authors.

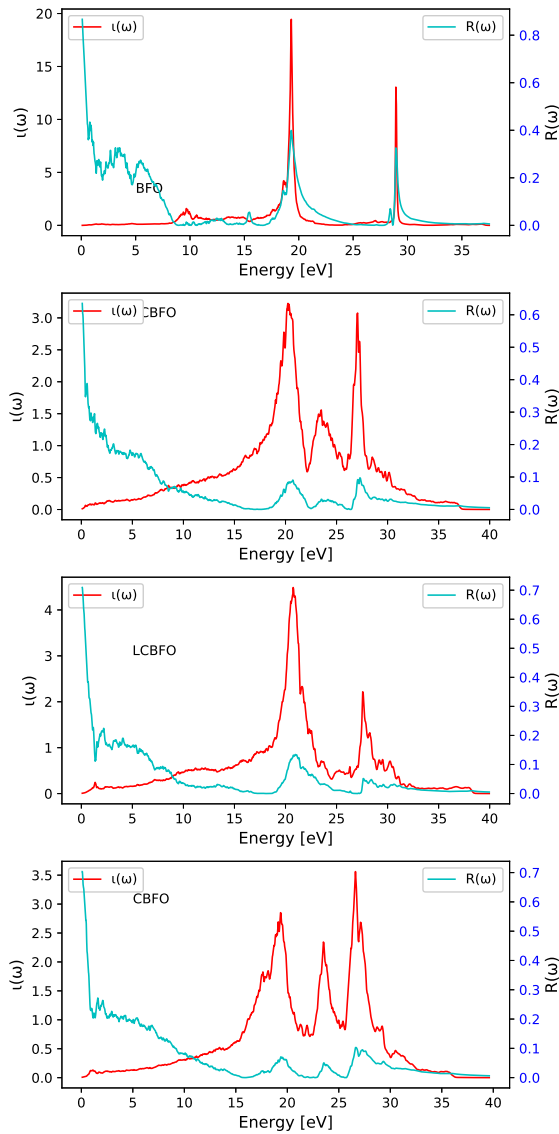


FIG. 6: The energy loss, $\iota(\omega)$ & reflectivity, $R(\omega)$ for pristine BiFeO₃ in comparison to doped BiFeO₃. (For color online, the reader is referred to the web version of this article).

ACKNOWLEDGEMENTS

We are grateful to the Ministry of Science and Higher Education of Ethiopia for financial support. The authors also acknowledge the Department of Physics at Addis Ababa University and the International Science Program, Uppsala University, Sweden, for providing computer facilities.

ORCID IDS

K.N. Nigussa.

<https://orcid.org/0000-0002-0065-4325>.

- ¹C.-H. Yang, D. Kan, I. Takeuchi, V. Nagarajan, J. Seidel, [High temperature phase transitions in tungsten trioxide-the last word?](#), J. Phys. Condensed Matter 13 (2001) 1.
- ²Q. Yang, Q. Xu, M. Sobhan, Q. Ke, F. Anariba, K. Ong, P. Wu, [Simultaneous reduction in leakage current and enhancement in magnetic moment in BiFeO₃ nanofibers via optimized Sn doping](#), physica status solidi (RRL)-Rapid Research Letters 8 (7) (2014) 653–657.
- ³S. Ameer, K. Jindal, M. Tomar, P. Jha, V. Gupta, [Effect of Li doping on the electronic and magnetic properties of BiFeO₃ by first principles](#), Integrated Ferroelectrics 193 (1) (2018) 123–128.
- ⁴A. Sen, M. Hasan, Z. Islam, M. Hassan, T. Zaman, M. Matin, F. Gulshan, [Influence of Ba and Mo co-doping on the structural, electrical, magnetic and optical properties of BiFeO₃ ceramics](#), Materials Research Express 7 (1) (2020) 016312.
- ⁵D. Arnold, [Composition-driven structural phase transitions in rare-earth-doped BiFeO₃ ceramics: a review](#), IEEE Transactions on Ultrasonics, Ferroelectrics, and Frequency Control 62 (1) (2015) 62–82.
- ⁶H. Tao, J. Lv, R. Zhang, R. Xiang, J. Wu, [Lead-free rare earth-modified BiFeO₃ ceramics: Phase structure and electrical properties](#), Materials and Design 120 (2017) 83–89.
- ⁷K. Nalwa, A. Garg, [Phase evolution, magnetic and electrical properties in Sm-doped bismuth ferrite](#), Journal of Applied Physics 103 (4) (2008) 044101.
- ⁸D. Kan, L. P. V. Anbusathaiah, C. Cheng, S. Fujino, V. Nagarajan, K. Rabe, I. Takeuchi, [Universal behavior and electric-field-induced structural transition in rare-earth-substituted BiFeO₃](#), Advanced Functional Materials 20 (7) (2010) 1108–1115.
- ⁹J. Schiemer, R. Withers, Y. Liu, M. Carpenter, [Ca-doping of BiFeO₃: The role of strain in determining coupling between ferroelectric displacements, magnetic moments, octahedral tilting, and oxygen-vacancy ordering](#), Chemistry of Materials 25 (21) (2013) 4436–4446.
- ¹⁰H. Hojo, K. Onuma, Y. Ikuhara, M. Azuma, [Structural evolution and enhanced piezoresponse in cobalt-substituted BiFeO₃ thin films](#), Applied Physics Express 7 (9) (2014) 091501.
- ¹¹L. Bai, M. Sun, W. Ma, J. Yang, J. Zhang, Y. Liu, [Enhanced magnetic properties of Co-doped BiFeO₃ thin films via structural progression](#), Nanomaterials 10 (9).
- ¹²R. Haumont, I. Kornev, S. Lisenkov, L. Bellaiche, J. Kreisel, B. Dkhil, [Phase stability and structural temperature dependence in powdered multiferroic BiFeO₃](#), Phys. Rev. B 78 (2008) 134108.
- ¹³U. Nuraini, S. Suasmoro, [Crystal structure and phase transformation of BiFeO₃ multiferroics on the temperature variation](#), Journal of Physics: Conference Series.
- ¹⁴J. Enkovaara, C. Rostgaard, J. Mortensen, J. Chen, M. Dulak, L. Ferrighi, J. Gavnholt, C. Glinsvad, V. Haikola, H. Hansen, H. Kristoffersen, M. Kuisma, A. Larsen, L. Lehtovaara, M. Ljungberg, O. Lopez-Acevedo, P. Moses, J. Ojanen, T. Olsen, V. Petzold, N. Romero, J. Stausholm-Møller, M. Strange, G. Tritsaridis, M. Vanin, M. Walter, B. Hammer, H. Häkkinen, G. Madsen, R. Nieminen, J. Nørskov, M. Puska, T. Rantala, J. Schiøtz, K. Thygesen, K. Jacobsen, [Electronic structure calculations with GPAW: a real-space implementation of the projector augmented-wave method](#), J. Phys.: Condens. Matter 22 (2010) 253202.
- ¹⁵J. Mortensen, L. Hansen, K. Jacobsen, [Real-space grid implementation of the projector augmented wave method](#), Phys. Rev. B 71 (2005) 035109.
- ¹⁶W. Kohn, L. Sham, [Self-consistent equations including exchange and correlation effects](#), Phys. Rev. 140 (1965) A1133–A1138.
- ¹⁷P. Blöchl, [Projector augmented-wave method](#), Phys. Rev. B 50 (1994) 17953.
- ¹⁸H. Monkhorst, J. Pack, [Special points for Brillouin-zone integrations](#), Phys. Rev. B 13 (1976) 5188.

- ¹⁹H. Schlegel, [Optimization of equilibrium geometries and transition structures](#), J. Comp. Chem. 3 (1982) 214.
- ²⁰P. Feynman, [Forces in Molecules](#), Phys. Rev. 56 (1939) 340.
- ²¹O. Nielsen, R. Martin, [Quantum-mechanical theory of stress and force](#), Phys. Rev. B. 32 (1985) 3780.
- ²²R. Wentzcovitch, J. Martins, [First principles molecular dynamics of Li: Test of a new algorithm](#), Solid State Commun. 78 (1991) 831.
- ²³J. Perdew, K. Burke, M. Ernzerhof, [Generalized Gradient Approximation Made Simple](#), Phys. Rev. Lett. 77 (1996) 3865.
- ²⁴A. Liechtenstein, V. Anisimov, J. Zaanen, [Density-functional theory and strong interactions: orbital ordering in mott-hubbard insulators](#), Phys. Rev. B 52 (1995) R5467.
- ²⁵S. Dudarev, G. Botton, S. Savrasov, C. Humphreys, A. Sutton, [Electron-energy-loss spectra and the structural stability of nickel oxide: an LSDA+U study](#), Phys. Rev. B 57 (1998) 1505.
- ²⁶A. MacDonald, S. Vosko, P. Coleridge, [Extensions of the tetrahedron method for evaluating spectral properties of solids](#), Journal of Physics C: Solid State Physics 12 (15) (1979) 2991–3002.
- ²⁷M. Hybertsen, S. Louie, [Ab initio static dielectric matrices from the density-functional approach: Formulation and application to semiconductors and insulators](#), Phys. Rev. B 35 (1987) 5585.
- ²⁸M. Gajdoš, K. Hummer, G. Kresse, J. Furthmüller, F. Bechstedt, [Linear optical properties in the projector-augmented wave methodology](#), Phys. Rev. B 73 (2006) 045112.
- ²⁹M. Shishkin, G. Kresse, [Implementation and performance of the frequency-dependent GW method within the PAW framework](#), Phys. Rev. B 74 (2006) 035101.
- ³⁰F. Wooten, Optical Properties of Solids, Academic Press, New York, 1972.
- ³¹A. Glass, D. v. Linde, T. Negran, [High-voltage bulk photovoltaic effect and the photorefractive process in LiNbO₃](#), Applied Physics Letters 25 (4) (1974) 233–235.
- ³²J. Tauc, R. Grigorovici, A. Vancu, [Optical properties and electronic structure of amorphous germanium](#), physica status solidi (b) 15 (2) (1966) 627–637.
- ³³T. Ada, K. Nigussa, L. Deja, [The effect of non-centrosymmetry on optical and electronic properties of BaHfO₃ perovskite](#), Computational Condensed Matter 26 (2021) e00524.
- ³⁴T. Shen, C. Hu, H. Dai, W. Yang, H. Liu, X. Wei, [First principles study of structural, electronic and optical properties of BiFeO₃ in ferroelectric and paraelectric phases](#), Materials Research Innovations 19 (sup5) (2015) S5–684–S5–688. <https://doi.org/10.1179/1432891714Z.0000000001176>
- ³⁵Z. Teng, J. Jiang, G. Chen, C. Ma, F. Zhang, [The electronic structures and optical properties of B, C or N doped BaTiO₃](#), AIP Advances 8 (9) (2018) 095216.
- ³⁶T. Olsen, [Designing in-plane heterostructures of quantum spin hall insulators from first principles: 1t′ – mos₂ with adsorbates](#), Phys. Rev. B 94 (2016) 235106.
- ³⁷P. Paufler, [International tables for crystallography](#), Acta Cryst. A63 (2007) 483.
- ³⁸S. Zhang, M. Lu, D. Wu, Y. Chen, N. Ming, [Larger polarization and weak ferromagnetism in quenched BiFeO₃ ceramics with a distorted rhombohedral crystal structure](#), Applied Physics Letters 87 (2005) 26.
- ³⁹Y. Hinuma, G. Pizzi, Y. Kumagai, F. Oba, I. Tanaka, [Band structure diagram paths based on crystallography](#), Comp. Mat. Sci. 128 (2017) 140.
- ⁴⁰Y.-T. Peng, S.-H. Chiou, C.-H. Hsiao, C. Ouyang, C.-S. Tu, [Remarkably enhanced photovoltaic effects and first-principles calculations in neodymium doped bifeo₃](#), Scientific Reports 7 (2017) 45104.
- ⁴¹J. Schilling, [The quest for zero refractive index](#), Nature Photonics 5 (8) (2011) 449–451.
- ⁴²I. Liberal, N. Engheta, [Near-zero refractive index photonics](#), Nature Photonics 11 (3) (2017) 149–158.